

# Imaging geologic surfaces by inverting gravity gradient data with depth horizons

Gary Barnes<sup>1</sup> and Joseph Barraud<sup>1</sup>

## ABSTRACT

The nonuniqueness problem that occurs when inverting potential field data is well known. It can, however, be surmounted by jointly inverting these data with independent data sets, incorporating depth information and regularizing the solution. The goal is to produce a geologic model that is compatible with all measured quantities, does not exceed any prescribed limits, and is geologically plausible. To achieve this, we have developed a spatially based surface inversion algorithm that solves for the geometric interface between geologic bodies. The bodies are constructed from grids of rectangular prisms that have their bottom depths adjusted by the algorithm to form the inverted surface. To solve large-scale inversions, approximations are used in the potential field calculations that allow internal ma-

trices to be stored in sparse format with minimal loss of accuracy. The impetus for the work came from the need to combine airborne gravity gradient data with depth horizons estimated from interpreted 2D seismic profiles to form a high-resolution 3D inversion for imaging salt bodies. By treating the depth information as measurements rather than constraints, we accommodate uncertainties in these estimates. Total variation regularization is incorporated to support the sharp edges of the salt structures and to stabilize the solution. Inversions for near-surface structures also incorporate a high-pass filter to suppress the interference in the gravity gradient signal from deeper geology. The resulting optimization finds a surface that fits (in a least-squares sense) the depth information and the high-frequency content of the gravity gradient data.

## INTRODUCTION

There is a variety of methods that have been used to invert gravity data into 3D geologic models. In all cases, the objective is to devise a model that honors constraints, produces fields that agree with available measurements, and is geologically plausible. Inversions can be performed manually by adjusting the geologic model by hand, or automatically using an optimization algorithm. Reviews of the different methods have been conducted by Oldenburg and Pratt (2007) and Barbosa and Silva (2010). Several algorithms (see, for example, Pilkington, 2006 or Li, 2010) have been based on the Fourier method using Parker's formula (Parker, 1973). Such implementations take advantage of the rapid forward calculations of gridded data via the Fast Fourier transform (FFT) and have formed the backbone of several commercial software products. In our own implementations of Fourier-based inversions, we have found it awkward to incorporate depth information and spatially control

the inverted surface. The alternative is the spatial method, which offers greater flexibility, but at the expense of computational efficiency. This approach appears in two strands: one where a 3D density distribution is sought and the other where the boundaries between geologic bodies of known or assumed density are determined. Incorporating depth information is more natural in a spatial implementation and similarly, spatial regularization can be used to control the inversion rather than filtering.

Fully 3D density inversions have been devised and successfully applied to a variety of geologic settings; see, for example, Fedi and Rapolla (1999), Zhdanov et al. (2004), Wan and Zhdanov (2008), Silva Dias et al. (2011). All these methods involve a discretization of the model space into 3D voxels resulting in very large, but linear optimization problems. By utilizing compression techniques, Portniaguine and Zhdanov (2002) show how the computational burden can be reduced to a manageable size. Li and Oldenburg (2003) utilize wavelet transforms and compression to yield efficient matrix-

Manuscript received by the Editor 19 April 2011; revised manuscript received 18 October 2011; published online 3 February 2012; corrected version published online 14 February 2012.

<sup>1</sup>ARKex Ltd., Cambridge, U. K. E-mail: gary.barnes@arkex.com, joseph.barraud@arkex.com.  
© 2012 Society of Exploration Geophysicists. All rights reserved.

vector multiplications. Other methods to increase the efficiency include making the discretization adaptive so that the vertical boundaries of the voxels are moved to the depths where the property is changing (Fullagar et al., 2008).

Spatial inversions for the surface defining the interface between geologic bodies have also been implemented and used on field data, see for example; Medeiros and Silva (1996), Barbosa et al. (1997). These methods minimize a nonlinear functional containing terms relating to the data misfit function and a regularizing function that imposes certain behavior on the surface. Our implementation follows a similar strategy, but the focus has been on incorporating the depth estimates from the interpretation of 2D seismic with gravity gradient data. Rather than incorporating the depth estimates as fixed constraints on the surface, we treat them as though they were a set of measurements. This allows uncertainties to be attributed to reflect the errors in these data that are caused by inaccurate velocity models or incorrect interpretations. The importance of considering these uncertainties was highlighted in the 2011 SEG honorary lecture given by Richard Lane where a 3D model built using gravity and magnetic data suggested a section of a 2D seismic line had been incorrectly interpreted (Lane, 2011). We couple the depth estimates with the gravity gradient data in a global optimization to form a single inversion for the surface. Both data sets invariably contain high-resolution information leading to large-scale optimization problems. By employing approximations in the field calculations, we show that the nonlinear surface inversion can be made computationally efficient even for the exploration sized airborne surveys commissioned by the oil industry.

The impetus for the work stemmed from a West African full tensor gravity gradient (FTG) survey over an area containing many salt structures. A sporadic set of 2D seismic lines had already been shot in this region, but with insufficient coverage, there was not enough information to form a complete geologic picture. Being shallow isolated features with large density contrasts, the salt bodies provided ideal signals for a gravity gradient survey. One of the objectives of the study was to image the top-salt surface by inverting the gravity gradient data with the top-salt horizons deduced from the depth-migrated seismic data. Results taken from this work are presented here to demonstrate the inversion technique.

Although the method equally applies to magnetic as well as gravity data (and even using both under the common source assumption), for reasons of clarity, the theory will be described in terms of gravity/gravity gradient data only. First, the basic inversion method is described, where a surface is solved for that simply fits the field measurements. The inversion is then embellished by introducing regularization and depth information, making it an optimization that produces a surface that not only fits the field measurements

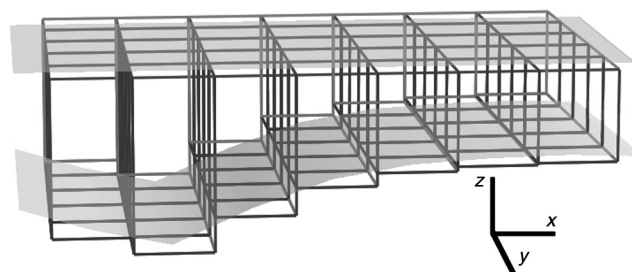


Figure 1. Discretization of geologic bodies into rectangular prisms.

but also fits the depth information and conforms to a prescribed behavior. We then incorporate a high-pass filter into the inversion and demonstrate how the interfering signal from deeper geology can be suppressed and prevented from corrupting the inversion of the target layer.

## METHOD

### Surface inversion

Figure 1 shows the discretization used to represent a geological body in the inversion model. It is based on a regular grid of rectangular prisms each with a prescribed density, a fixed top, and an adjustable bottom. This type of discretization, being grid based, is computationally convenient, but cannot represent multi- $z$  surfaces, and therefore, precludes the possibility of inverting structures such as thrust faults or overhanging salt domes.

The gravity response  $f_{\text{block}}$  from the  $j$ th block at the  $i$ th field point  $\mathbf{r}_i$  is a function of the block geometry ( $x_{1j}, x_{2j}, y_{1j}, y_{2j}, z_{1j}, z_{2j}$ ) and density  $\rho_j$ . The total response of the model  $F_i$  is then the sum over all the  $N$  individual blocks:

$$F_i = \sum_{j=1}^N f_{\text{block}}(\mathbf{r}_i, \rho_j, x_{1j}, x_{2j}, y_{1j}, y_{2j}, z_{1j}, z_{2j}). \quad (1)$$

A least-squares fit to a set of measurements  $m_{i=1\dots M}$  can be stated as follows:

$$\text{Minimize} \left\{ \sum_{i=1}^M (F_i - m_i)^2 \right\}, \quad (2)$$

where, for this surface inversion, the minimization is with respect to the depth of the block bottoms,  $z_{1j}$ . Because  $f_{\text{block}}$  is a nonlinear function of  $z_{1j}$ , the problem falls into the category of nonlinear optimization. To solve this minimization, the field from each block is approximated by a Taylor expansion with respect to the change in the bottom surface  $\Delta z_{1j}$  about the current position  $z_{1j}$ :

$$f_{\text{block}}(z_{1j} + \Delta z_{1j}) \approx f_{\text{block}}(z_{1j}) + \frac{\partial f_{\text{block}}}{\partial z_{1j}} \Big|_{z_{1j}} \Delta z_{1j} + O(\Delta z_{1j})^2. \quad (3)$$

Using this truncated expansion, the nonlinear optimization (equation 2) can be approximated by a series of linear steps, each solving for an incremental change  $\Delta z_{1j}$  in the surface. Each step minimizes the residual between the current solution's forward calculation  $\mathbf{F}_0$  and the measurements:

$$\begin{aligned} &\text{minimize } f(\Delta \mathbf{z}_1) \\ &f(\Delta \mathbf{z}_1) = (\mathbf{A} \Delta \mathbf{z}_1 - (\mathbf{m} - \mathbf{F}_0))^2, \end{aligned} \quad (4)$$

where  $\mathbf{A}$  is the Jacobian matrix having elements  $A_{i,j}$  representing the derivative of the field due to block  $j$  at measurement  $i$ , and  $\Delta \mathbf{z}_1$  is a vector of the incremental depth changes. Here,  $\mathbf{F}_0$  can be referred to as the datum response, being the field forward-calculated from the model before perturbation (that is with  $\Delta \mathbf{z}_1 = \mathbf{0}$ ). Equations for the vertical gravity ( $g_z$ ) and gravity gradient ( $G_{zz}$ ) from a rectangular block element and their associated derivatives with respect to  $z_{1j}$  are given in the appendix. Being a linear step, the optimization (equation 4) can be solved using the standard conjugate

gradient algorithm. After each solution, the datum response is recalculated and the next linear step is solved. The process stops when the elements of the vector  $\Delta\mathbf{z}_1$  are sufficiently small to indicate convergence.

The truncation to the linear term in equation 3 is a good approximation because the inverting surface, being the bottom of the geological body, often implies a suitably large distance between the points of expansion and the field points,  $|z_1| \gg |\Delta z_1|$ .

For typical geological applications in oil exploration, the matrix  $\mathbf{A}$ , having as many rows as there are measurements and a number of columns equal to the number of blocks in the inversion, can become so large that the solution becomes impracticable. To make the problem tractable, an approximation is made so that blocks distant from the field point can be averaged together to form larger blocks thereby accumulating many matrix elements into a single averaged element. The averaged block has a top surface, bottom surface, and density all being the averages of the blocks in which it encompasses. A recursive algorithm decides how to group the blocks together to generate a new  $\mathbf{A}$  matrix that is sparse with occupancy typically less than 1%. This algorithm and the mechanisms by which the sparse matrix is implemented into the conjugate gradient solver are described by Barnes and Lumley (2011). Figure 2b shows how the model resolution decreases as a function of distance from a particular field point. At the field point (located above the center of the model in Figure 2), there is negligible difference between the field calculated from the full resolution (Figure 2a) model and the approximate model (Figure 2b).

During the inversions, to prevent the bottom surface from rising above the body's top surface, we build in an intrinsic inequality constraint stating that the bottom must be below the top. To achieve this, we adopt the simple method of projecting the solution onto the constraint boundaries during the iterations of the conjugate gradient solver (Press et al., 1997). This can, however, make the inversion unstable. When constraint boundaries are active, we employ undershooting to help stabilize the solver by making the solution approach the boundaries more gradually:

$$\Delta z_1 \rightarrow \alpha \Delta z_1, \quad (5)$$

where  $\alpha < 1$  is the undershooting or deceleration factor.

## Regularization

A regularization function is an essential component when inverting potential field data. It not only improves the stability and integrity of the inversion, but also provides a method for controlling the behavior of the inversion to steer it toward geologically meaningful solutions.

The regularization adds into the minimization (equation 4) in the style of a Lagrange function,  $R(\mathbf{z}_1 + \Delta\mathbf{z}_1)$ :

Minimize  $f(\Delta\mathbf{z}_1)$

$$f(\Delta\mathbf{z}_1) = (\mathbf{A}\Delta\mathbf{z}_1 - (\mathbf{m} - \mathbf{F}_0))^2 + \lambda R(\mathbf{z}_1 + \Delta\mathbf{z}_1), \quad (6)$$

where  $\lambda$  is the associated regularization factor (Lagrange multiplier) that controls the level of compliance with the regularization relative to the fit to the measurements. A common method is the Tikhonov maximum smoothness, which penalizes the inversion against the surface gradient energy:

$$R_{MS}(\mathbf{z}) = \nabla(\mathbf{z})^T \nabla(\mathbf{z}). \quad (7)$$

Being quadratic in form it is readily incorporated into gradient based solvers alongside the least-squares fit to the measurements. It can be geologically representative in some situations when surfaces mimicking rolling hills are sought and discontinuities or sharp boundaries are not expected. However, in many exploration projects, it can blur out the features of interest and make the solutions too unrealistic.

Martins et al. (2011) and Lima et al. (2011) demonstrate the suitability of using total variation (TV) regularization for modeling discontinuous features such as faults or steep-sided basins. The TV function (Acar and Vogel, 1994), is given by

$$R_{TV}(\mathbf{z}) = \sum_{i=1}^N \sqrt{|\nabla z_i|^2 + \beta} \quad (8)$$

where  $\beta$  is a small number introduced to ensure differentiability.

Rather than following the method of Martins et al. (2011) and incorporating this nonlinear functional into the Gauss-Newton style minimization (equation 6), as a second Jacobian matrix, we treat it as a pseudoquadratic functional following Zhdanov (2002) allowing us to incorporate it directly into the conjugate gradient algorithm. Each Gauss-Newton step then involves solving the linearized ex-

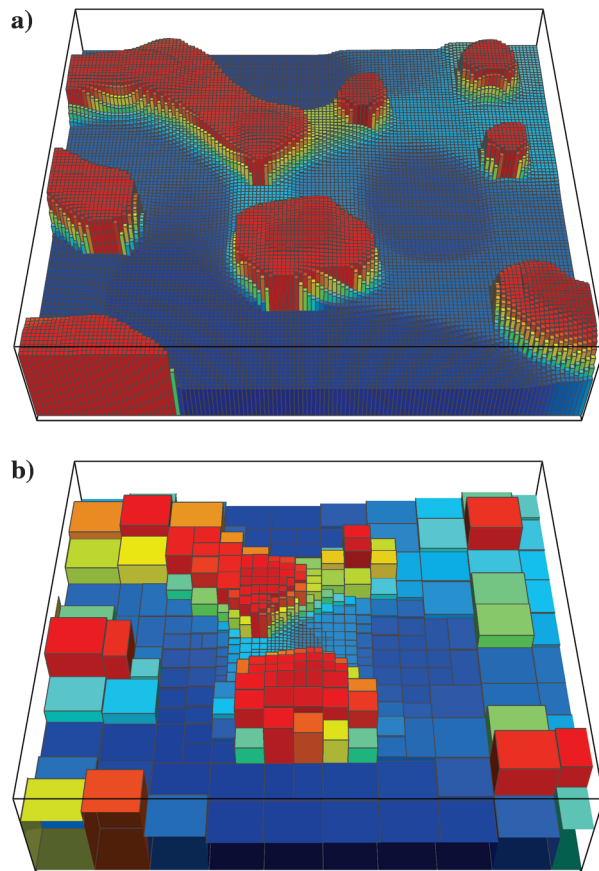


Figure 2. Approximation of the field calculation. (a) Body with full resolution, (b) adaptive resolution for a field point above model center.

pansion of the field with the nonlinear TV regularization function. The high computational cost associated with recalculating the field Jacobian matrix  $\mathbf{A}$  makes the fully nonlinear conjugate gradient solution undesirable, but because the linear expansion is generally a good approximation, the combined linearized field and nonlinear regularization scheme is efficient. Typically, inversions require around 5–10 iterations of equation 6, each involving a few hundred conjugate gradient search directions.

The search directions in the conjugate gradient algorithm are formed by evaluating the gradient of the functional in equation 6,

$$\nabla f(\Delta \mathbf{z}_1) = 2\mathbf{A}^T(\mathbf{A}\Delta \mathbf{z}_1 - (\mathbf{m} - \mathbf{F}_0)) + \lambda \frac{\partial R(\mathbf{z}_1 + \Delta \mathbf{z}_1)}{\partial \Delta \mathbf{z}_1}, \quad (9)$$

and combining with the previous direction to form a set of conjugate directions (see Zhdanov, 2002 for details). The derivative of  $R_{TV}$  is given by

$$\frac{\partial R_{TV}}{\partial \mathbf{z}} = \mathbf{G}_x^T \mathbf{a}_x + \mathbf{G}_y^T \mathbf{a}_y, \quad (10)$$

where  $\mathbf{G}_x$  and  $\mathbf{G}_y$  are the  $x$ - and  $y$ -differential matrix operators, and vectors

$$\begin{aligned} \mathbf{a}_x &= \frac{\mathbf{G}_x \mathbf{z}}{\sqrt{(\mathbf{G}_x \mathbf{z})^2 + (\mathbf{G}_y \mathbf{z})^2 + \beta}}, \\ \mathbf{a}_y &= \frac{\mathbf{G}_y \mathbf{z}}{\sqrt{(\mathbf{G}_x \mathbf{z})^2 + (\mathbf{G}_y \mathbf{z})^2 + \beta}} \end{aligned} \quad (11)$$

are the normalized derivatives of  $\mathbf{z}$  (see Martins et al., 2011 for a derivation). Notice that if  $\beta$  is increased toward infinity, equation 10 starts to resemble the derivative of the maximum smoothness function (equation 7). Consequently,  $\beta$  can be used to control a blend between the TV and maximum smoothness regularization schemes.

When treating the regularization as a pseudoquadratic functional, equation 10 is expressed as though it were a vector of constant coefficients that multiply the variables  $\mathbf{z}$ . This is achieved by essentially dividing it by  $\mathbf{z}$ , allowing another  $\mathbf{z}$  to be factorized out,

$$\frac{\partial R_{TV}}{\partial \mathbf{z}} \rightarrow \left[ (\mathbf{G}_x^T \mathbf{a}_x + \mathbf{G}_y^T \mathbf{a}_y) \frac{\mathbf{z}}{\mathbf{z}^2 + e} \right] \mathbf{z}, \quad (12)$$

where  $e$  is a small number to prevent a division by zero. The term in square brackets represents the pseudoquadratic Tikhonov style regularization vector that is used within the conjugate gradient algorithm and is re-evaluated for each search direction.

### Incorporating depth information

We treat the depth estimates as though they represent a set of measurements of the geological surface. From an implementation point-of-view, we incorporate them in the same way as the potential field data. The block kernel function  $f_{block}$ , when associated with depth estimates, becomes an interpolation forward calculation function rather than a potential field kernel. A simple interpolation function to use is the inverse distance weighted average:

$$h_i(\mathbf{r}_i) = \frac{\sum_{j=1}^N \frac{z_j}{r_{i,j}^n}}{\sum_{j=1}^N \frac{1}{r_{i,j}^n}}, \quad (13)$$

where  $h_i$  are the interpolated model surface heights at the  $x, y$  locations,  $\mathbf{r}_i$  of the depth estimates,  $r_{i,j}$  is the  $x$ - $y$  distance between the center of the  $j$ th model block and the  $i$ th measurement, and  $n$  is the order of the interpolation. Equation 13 forward calculates the model surface heights to the  $x, y$  locations of the estimates, just as equation 1 would forward calculate the gravity to the  $x, y, z$  field points. Increasing  $n$  makes the interpolator more localized to the model blocks that are closest to the measurement positions and during the inversion loosely controls the distance over which a depth estimate influences the model. In practice, the summation is truncated to include only the most dominant terms.

After specifying a forward calculation by means of an interpolation function, the inverse problem of finding a surface given a sporadic set of depth measurements can be defined:

$$\begin{aligned} &\text{Minimize } s(\Delta \mathbf{z}_1) \\ &s(\Delta \mathbf{z}_1) = (\mathbf{T}(\Delta \mathbf{z}_1 + \mathbf{z}_1) - \mathbf{d})^2, \end{aligned} \quad (14)$$

where matrix  $\mathbf{T}$  represents the interpolation function in equation 13:

$$T_{i,j} = \frac{\frac{1}{r_{i,j}^n}}{\sum_{j=1}^N \frac{1}{r_{i,j}^n}}, \quad (15)$$

and vector  $\mathbf{d}$  contains the measurements or estimates of surface depth. This optimization problem, expressed as a least-squares fit to the depth data is equivalent to the method of gridding aeromagnetic data through inverse interpolation adopted by Guo et al. (2011).

Equations 6 and 14 are combined to form a global optimization,

$$\text{Minimize } f(\Delta \mathbf{z}_1)$$

$$f(\Delta \mathbf{z}_1) = \left( \begin{bmatrix} \mathbf{A} \\ \mathbf{T} \end{bmatrix} \Delta \mathbf{z}_1 - \begin{bmatrix} \mathbf{m} - \mathbf{F}_0 \\ \mathbf{d} - \mathbf{Tz}_1 \end{bmatrix} \right)^2 + \lambda R(\mathbf{z}_1 + \Delta \mathbf{z}_1), \quad (16)$$

where  $\begin{bmatrix} \mathbf{m} - \mathbf{F}_0 \\ \mathbf{d} - \mathbf{Tz}_1 \end{bmatrix}$  represents an augmented measurement residual vector, having the potential field measurements followed by the depth information.

To control the relative importance of different measurements, a diagonal weight matrix  $\mathbf{W}$  can be added to the cost functional:

$$\begin{aligned} f(\Delta \mathbf{z}_1) &= \left( \mathbf{W} \left( \begin{bmatrix} \mathbf{A} \\ \mathbf{T} \end{bmatrix} \Delta \mathbf{z}_1 - \begin{bmatrix} \mathbf{m} - \mathbf{F}_0 \\ \mathbf{d} - \mathbf{Tz}_1 \end{bmatrix} \right) \right)^2 \\ &\quad + \lambda R(\mathbf{z}_1 + \Delta \mathbf{z}_1). \end{aligned} \quad (17)$$

By assigning relatively larger weights to the elements of  $\mathbf{W}$  that correspond to the depth estimates, the inversion can be forced to honor these measurements more closely than the potential field data. This is appropriate when the depth estimates are known to be accurate (from well logs, for example) and the data can be considered to act like hard constraints in the inversion. In general, one can achieve more accurate models by treating the depth information as estimates and specifying their appropriate uncertainties in the

weighting matrix  $\mathbf{W}$ . In the field example, which uses depth information from interpreted 2D seismic, we trust, and therefore weight relatively higher, the shallower estimates more than the deep estimates. The inversion can therefore be made to follow the reliable depth horizons more closely and, if required to fit the gravity gradient data, allow possibly more departure from the horizons when they are more uncertain.

## Focused inversion

If the goal of a surface inversion is to deduce a deep basement horizon, then inverting on gravity data rather than gravity gradient data can be preferential. In the case of a gravity gradient survey, this would mean transforming the  $G_{zz}$  data into  $g_z$  using vertical integration and possibly merging in regional data to conform the long wavelengths (Dransfield, 2010). Gravity fields, being less sensitive to the near-surface sources, will automatically focus an inversion's optimization to fit the long-wavelength signal and be less affected by the high-frequency content from shallower geology. If the goal of an inversion is to image a shallower surface, then inverting on  $G_{zz}$  would be more logical. These choices are dictated by the distribution of spectral power in the respective components. Gravity gradient fields, having a more even distribution of power across a wider bandwidth, are more useful for shallow inversions. Transforming the measurements between gravity and gravity gradient can therefore be used to focus the inversion on different parts of the signal bandwidth.

One of the challenges in interpretation projects is to try and separate the signals from shallow and deep geology. The long-wavelength signal originates from both deep and shallow sources, but due to the exponential upward continuation factor in potential fields, the short-wavelength content is normally dominated by the near-surface sources. Short-wavelength signals can therefore be considered as unique to the shallow geology. By inverting a shallow surface using  $G_{zz}$ , one can, to a degree, eliminate the signal interference from the deeper sources.

Choosing to invert on  $G_{zz}$  or  $g_z$  is equivalent to incorporating a transformation within the inversion solver that modifies the residual to give a  $G_{zz}$  or  $g_z$  fit as required. To further emphasize the spectral separation, a technique we term as "focused inversion" can be employed to concentrate the inversion over specified frequency bands by employing filters rather than transformations. This term should not be confused with the term "image focusing" coined by Portniaguine and Zhdanov (1999) which concerns regularization. Our method parallels an idea in control theory and the technique of system identification where one can deduce more accurate system parameters by choosing appropriate frequency bands over which to model measured data. In geophysics, the idea has been used to determine more accurate density values for complex terrain corrections (Barnes et al., 2008). To focus an inversion on the high-frequency signal content, we incorporate a high-pass filter so that the solution essentially ignores the long-wavelength gravity signal altogether and fits to the bandwidth unique to the near-surface:

$$f(\Delta\mathbf{z}_1) = \left( \mathbf{W} \text{Filter} \left( \begin{bmatrix} \mathbf{A} \\ \mathbf{T} \end{bmatrix} \Delta\mathbf{z}_1 - \begin{bmatrix} \mathbf{m} - \mathbf{F}_0 \\ \mathbf{d} - \mathbf{Tz}_1 \end{bmatrix} \right) \right)^2 + \lambda R(\mathbf{z}_1 + \Delta\mathbf{z}_1), \quad (18)$$

where  $\text{Filter}()$  represents the filtering function or operator that acts on the residual in accordance with Agerlin's principle to ensure that

the measurements and model responses are treated in exactly the same way (Jacobsen, 1988).

The longer wavelengths in the inverted surface, are then controlled by the complementary data sets (for example, depth estimates), without being corrupted by the ambiguous long-wavelength gravity signal. This is not the same as just filtering the input data, but is equivalent to applying a frequency dependent weighting scheme. In basement inversions, Chakravarthi and Sundararajan (2007) accommodate interfering long-wavelength gravity variation by incorporating a spatial polynomial trend model into the inversion, thus making their inverted basement model immune to the background field. We have also found this method effective in removing the interference from deep geology when low-order polynomials suffice, but find higher order polynomials difficult to control when trying to accommodate more intermediate wavelengths (of the order of 10 km, for example) and prefer the filtering approach in these cases. In our spatial algorithm, the filter function in equation 18 can take the form of a multiplying matrix operator  $\mathbf{P}$ , acting as a filter in the convolution sense for the gravity residual and an identity matrix  $\mathbf{I}$ , to leave the residual of the depth estimates unchanged:

$$f(\Delta\mathbf{z}_1) = \left( \mathbf{W} \begin{bmatrix} \mathbf{P} & \mathbf{0} \\ \mathbf{0} & \mathbf{I} \end{bmatrix} \left( \begin{bmatrix} \mathbf{A} \\ \mathbf{T} \end{bmatrix} \Delta\mathbf{z}_1 - \begin{bmatrix} \mathbf{m} - \mathbf{F}_0 \\ \mathbf{d} - \mathbf{Tz}_1 \end{bmatrix} \right) \right)^2 + \lambda R(\mathbf{z}_1 + \Delta\mathbf{z}_1). \quad (19)$$

An exponential high-pass filter for the field measurements  $\mathbf{m}_i$  can be realized with matrix elements:

$$P_{i,j} = \delta_{i,j} - \frac{e^{-(r_{i,j}/\lambda_c)^n}}{\sum_{j=1}^M e^{-(r_{i,j}/\lambda_c)^n}}, \quad (20)$$

where  $\delta_{i,j} = 1$  if  $i = j$ ,  $\delta_{i,j} = 0$  if  $i \neq j$ ,  $r_{i,j}$  is the  $x$ - $y$  distance between field measurements  $i$  and  $j$ ,  $\lambda_c$  is the filter cut-off half-wavelength, and  $n$  is the filter order. As with the inverse distance interpolation function, when the distance  $r_{i,j}$  is sufficiently large, the matrix element can be assumed to be zero, thus making a sparse matrix.

## SYNTHETIC TEST

To demonstrate the above inversion technique, we have constructed a geological model consisting of three salt bodies intruding a limestone layer. The model was designed to act as a feasibility test for the field data inversion (see next section). Figures 3 and 4 show the 3D salt surface and a cross section through the model that runs perpendicular to an underlying basement graben. The top of the model consists of a 100-m-thick layer of low density ( $2.0 \text{ g/cm}^3$ ) sediment that sits on top of limestone whose density increases linearly with depth from  $2.45 \text{ g/cm}^3$  reaching  $2.6 \text{ g/cm}^3$  at 2000 m depth. We calculate the field from a model block with a depth-dependent density by splitting it up into discrete elements and integrating numerically. The numerical approach provides the flexibility to incorporate more complex density-depth relationships (the field example uses an exponential relation) or even lookup tables into the model. The salt has a uniform density of  $2.16 \text{ g/cm}^3$  and is situated over a basin that has been tilted. The edges of the model extend outward to infinity making the layers continuous to prevent edge effects in the forward calculations.

The target for the inversion test was to deduce the top-salt surface using the top-salt depths along the four profiles shown in Figure 3 and the  $G_{zz}$  data set forward-calculated from the entire model at 100 m altitude. The  $G_{zz}$  data (Figure 5) were corrupted with 100 m upward-continued random noise, scaled to have an rms fluctuation of 1 Eötvös indicative of the noise expected from processed FTG data flown with a tight line spacing of 150 m (Barnes et al., 2011). The four top-salt depth profiles were not corrupted by noise, but were assumed to represent accurately depth-migrated and interpreted 2D seismic data.

For the inversion, a single body representing the salt intruded limestone was defined as having a fixed top surface at 100 m depth, a positive depth-dependent density-contrast consistent with the limestone-salt interface and a base surface representing the bottom limestone surface (or equivalently, the top-salt). This surface was initialized at a depth of 1500 m to set the starting conditions of the inversion. The basement graben dominates the regional  $G_{zz}$  variation by producing a diagonal low running southwest–northeast in Figure 5. To prevent this from corrupting the single layer inversion, we introduced a focusing high-pass filter (equation 17) with a 4-km

cut-off wavelength. The cut-off wavelength ensures that the inversion only fits to the  $G_{zz}$  spectral content that originates predominantly from the near-surface target geology. In the regions away from the shallow salt structures, where there is little high-frequency  $G_{zz}$  signal, the trends in the inverted surface are governed by the depth information along the four profile lines. Here, the lack of high-frequency  $G_{zz}$  signal together with the regularization acts to interpolate the depth horizons in a plausible way. An unrealistic localized fit to the depth horizons is prevented because this would produce a high-frequency  $G_{zz}$  model response which would appear in the focused  $G_{zz}$  residual. Such a residual would be minimized by the solver by adjusting the surface to form a smooth interpolation in between the depth horizons. Without the focusing filter, the  $G_{zz}$  data and the depth information would contradict each other because the long-wavelength  $G_{zz}$  signal from the underlying graben would be wrongly attributed to the salt layer and force it to levels far away from those indicated by the depth profiles. Figure 6 illustrates this by showing the unfocused inversion of the  $G_{zz}$  data which resulted in a surface that accommodates the entire signal and is therefore distorted by the long wavelengths from the deeper geology. Simply

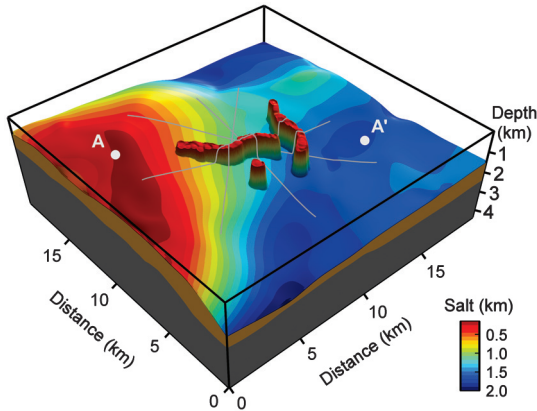


Figure 3. Synthetic test model. Positions of 2D depth profiles are shown as gray lines. Layers above the salt have been omitted for clarity.

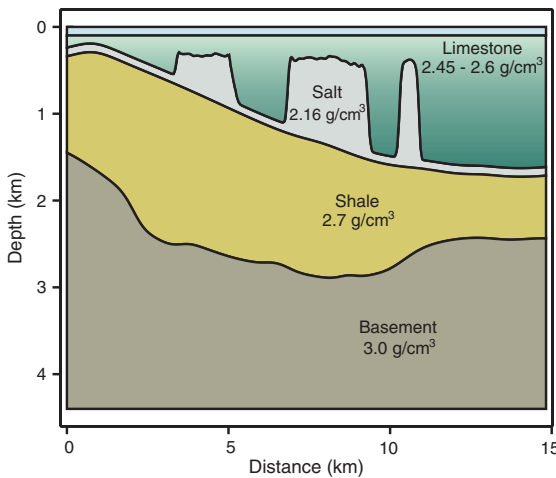


Figure 4. Cross section through synthetic model along the line defined by A–A'.

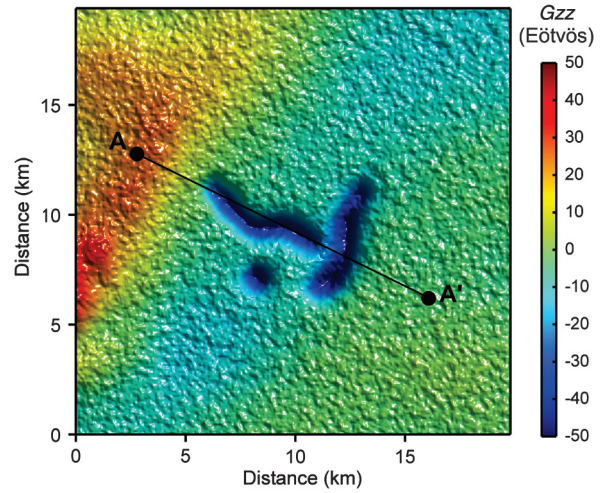


Figure 5. Synthetic  $G_{zz}$  data with noise representative of an airborne survey.

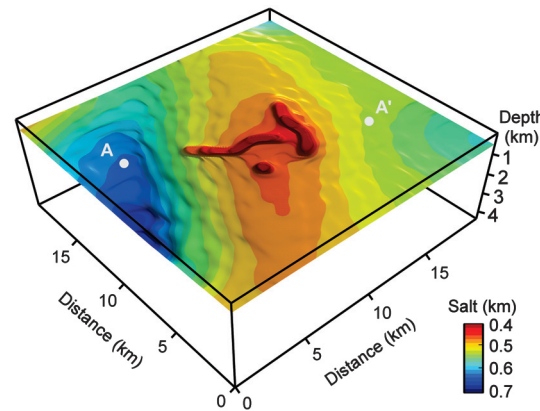


Figure 6. Corrupted top-salt surface resulting from the inversion of  $G_{zz}$  data without a focusing filter.

high-pass filtering the  $G_{zz}$  input data set also produces a bad solution. In this case, the inversion would be forced to fit to a gravity gradient field which (unknown to the solver) has had the long-wavelength components set to zero. Long-wavelength variations would therefore be prohibited in the inverted surface (because these would produce long-wavelength field components). Consequently, a sensible interpolation of the depth horizons would be prevented. The focusing filter, which operates on the  $G_{zz}$  residual within the optimization, resolves the conflict in the inversion and ensures that the surface conforms only to the relevant (near-surface) part of the signal bandwidth. Total variation regularization was used to stabilize the inversion and also to favor solutions having steep sided edges as discussed earlier.

Figure 7 shows the deduced top-salt solution from the focused inversion which incorporated both the depth data and the  $G_{zz}$  data. The solution reproduces the true surface very well and is most accurate in the central region where the availability of both depth information and high-frequency  $G_{zz}$  data allowed both data sets to take part in the inversion. Toward the edges of the model, which are not sampled by the depth profiles and do not contain high-frequency  $G_{zz}$  signal, the solution is more of an interpolation steered by the regularization, and therefore, represents a plausible, but not necessarily accurate, variation. Figure 8b and 8c compares the inversion results with the original model along the A-A' profile showing how the salt bodies, together with the underlying tilt of the near-surface layer have been inverted correctly. The inverted model can be used to forward calculate a near-surface correction for the original  $G_{zz}$  data. This forward calculation does not incorporate a filter. Even though the inversion only used the high-frequency part of the  $G_{zz}$  data, because the inverted model is accurate over a wide bandwidth, it can be used to predict both the high-frequency and long-wavelength near-surface signals. The near-surface corrected data is shown in Figure 8a and represents the signal from the deeper geology and could be used in further inversions to estimate the shale (base-salt) and basement layers. The correspondence of the solution with the model truth confirms the success of the inversion.

## FIELD EXAMPLE

During 2007–2008, ARKeX Ltd. conducted an airborne FTG survey over an onshore Gabon block. The study area was located along a clear trend of oil and gas subsalt fields that runs roughly

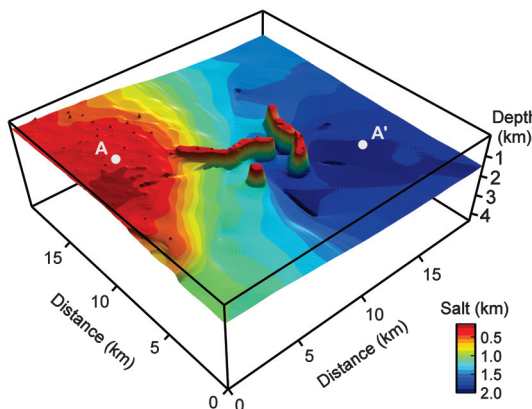


Figure 7. Top-salt surface resulting from the combined focused inversion of  $G_{zz}$  data and 2D depth horizons.

north–south from offshore fields in south Gabon to the Lambaréne horst in the north. As a proven reservoir rock, the primary objective is the Gamba Formation, which is overlain by the Ezanga Salt formation. The rest of the stratigraphy consists mainly of the Madiela limestone and dolomite, as well as recent detritic sediments. The salt forms large domes and walls intruding the limestone and are typically more than 1 km high and 2 km wide. A series of 2D seismic lines had been shot over this area, but due to environmental restrictions, the coverage was sporadic.

The FTG survey was conducted with a tight-line spacing of 150 m, necessary to image the finest detail in the near-surface structures. The full tensor data were processed using the equivalent-source technique described by Barnes and Lumley (2011) to reduce all the tensor components into an enhanced  $G_{zz}$  data set projected onto a level grid. The data were terrain corrected using a constant-density terrain model built using a LiDAR derived digital elevation model. Figure 9 shows the resulting signal and positions of 10 of

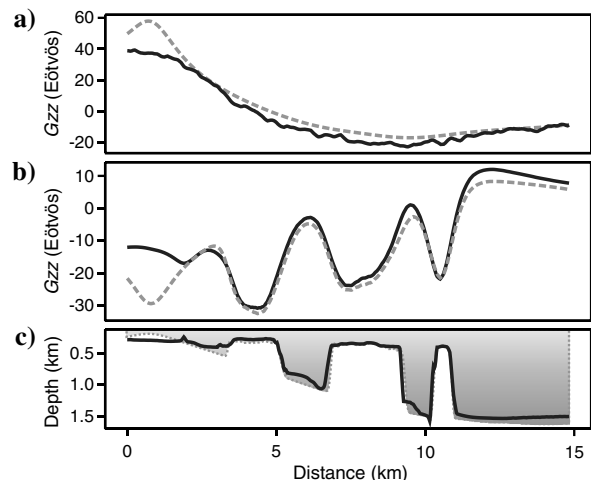


Figure 8. (a) Near-surface corrected  $G_{zz}$  data at 100 m altitude above profile line A-A', (b)  $G_{zz}$  from the limestone-salt interface, (c) limestone-salt interface, shaded region shows limestone layer. In all cases, the solid line is the inversion result and the dashed line is the exact answer.

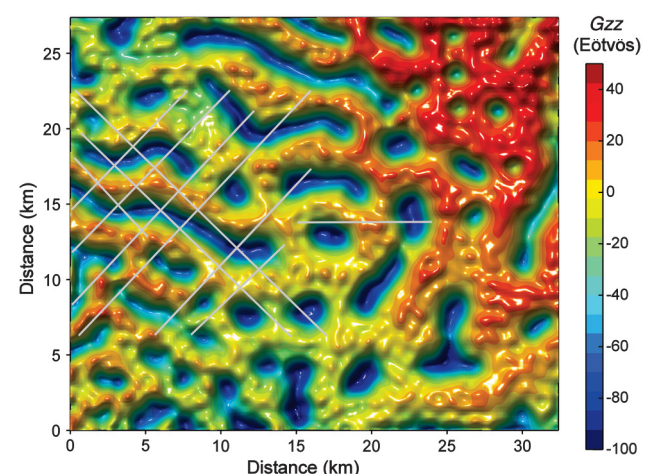


Figure 9. Gabon survey terrain corrected  $G_{zz}$  signal and locations of ten 2D seismic profiles.

the 2D seismic lines selected for use in this study. One can see that the high-frequency content of these anomalies and the relatively sparse sampling provided by the seismic lines meant that the seismic data alone were not able to image the features correctly.

In this case, it was preferable to use the processed and terrain corrected  $G_{zz}$  data for the inversion, rather than inverting directly for the six observed tensor components measured by the FTG. The processing methodology combines all the gradient measurements together using a technique that reduces noise and can also remove time-domain drift from the survey data. The resulting  $G_{zz}$ , therefore provided a more accurate input data set for use in this modeling. Further to this, by reducing all the measurements to a single component, the problem size could be kept to a minimum because the reprojected  $G_{zz}$  data set alone supports the signal and bandwidth of all six original data sets.

The conversion of the seismic reflections into depth was known to be erroneous due to the lack of an accurate velocity model and the 3D nature of the geology causing many out-of-plane reflections. The seismic data were improved by manually adjusting the depth

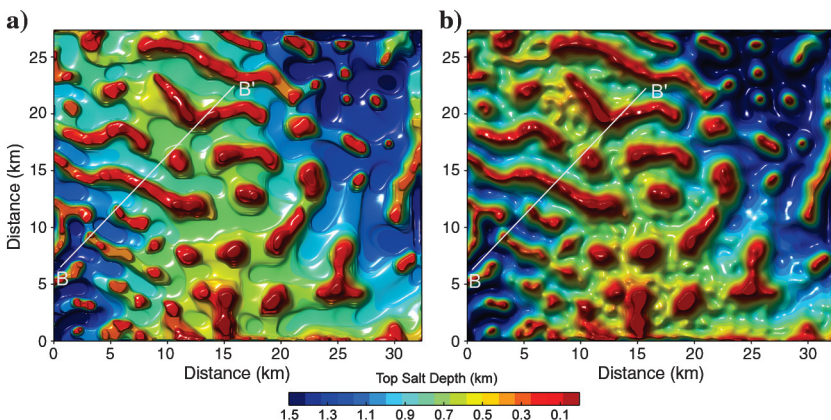


Figure 10. Unfocused surface inversions using only  $G_{zz}$  data. (a) Total variation regularization, (b) maximum smoothness regularization.

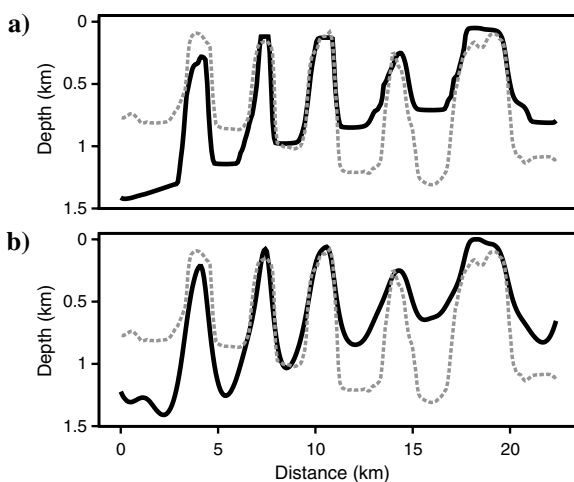


Figure 11. Comparison of unfocused  $G_{zz}$  inversions (solid lines) with 2D seismic derived top-salt (dashed lines) along profile B–B'. (a) Total variation regularization, (b) maximum smoothness regularization.

data so that 2D density models under each profile became compatible with the gravity gradient measurements and also honored available well information. This yielded an improved velocity model, which was iterated with the depth migration process resulting in an improved depth model, see Barraud et al. (2010) for further details. The full interpretational study of this area involved analyzing magnetic and regional gravity data together with the gravity gradient and seismic data to produce a complete model of the geology from the weathering layer above the salt, down to the basement. Here, following the synthetic test, we only present the inversion for the top-salt target.

The inversion model was formed by a single body constructed with  $433 \times 366$  grid cells each with size  $75 \times 75$  m. The top surface was placed at the lowest point of the terrain and the inverting bottom surface was initialized 500 m below. The assigned density contrast is consistent with a limestone-salt interface varying exponentially with depth from  $0.25 \text{ g/cm}^3$  at the top with an exponential length scale of 1 km:

$$\rho(s) = 0.25 + 0.5(1 - e^{-s}), \quad (21)$$

where  $s$  is the depth from the top surface in km. The parameters for this relation were chosen based on geologic expectations and tuned to achieve a consistent inversion when using both the gravity gradient data and the seismic derived top-salt depths.

Figure 10 compares the total variation and maximum smoothness regularized solutions where only the  $G_{zz}$  data were used without any focusing filters or depth information. In both cases, the regularization factors were adjusted to give roughly the same 3 E rms fit to the  $G_{zz}$  data (this residual is dominated by geologic noise rather than instrument noise). Figure 11 shows the inverted surfaces profiled along one of the seismic lines. Despite the nonuniqueness problem when inverting potential field data alone, these inverted surfaces show remarkable correspondence with the independent seismic top-salt interpretation. Comparing Figure 11a and 11b, one can see clearly that TV regularization is the appropriate choice for this setting because its steep sided salt bodies follow the seismic data much more closely. The discrepancies in the general trend of the inverted surfaces in between the salt bodies (the inverted surfaces trend upward along B–B' whereas the seismic horizon trends downward) are due to the corruption of the unfocused inversion by the long-wavelength signals from the deeper geology. This interference is also seen in Figure 10a and 10b where the bulging high in the inverted salt surface reflects the fitting to the long-wavelength signal from an underlying graben.

As in the synthetic example, we incorporated the 2D top-salt horizons into the inversion to control the long wavelengths and introduced the 4-km high-pass focused inversion filter to eliminate the deeper geology from the  $G_{zz}$  signal and to prevent a conflict between these two data sets during their combined inversion. In this case however, the seismic derived depth estimates are believed to be less reliable in between the salt bodies. This is for three reasons, (1) the deeper depths exercise more of the velocity model and are therefore more sensitive to its accuracy, (2) the deeper returns can be more corrupted by the out-of-plane sources, and (3) the top-salt pick

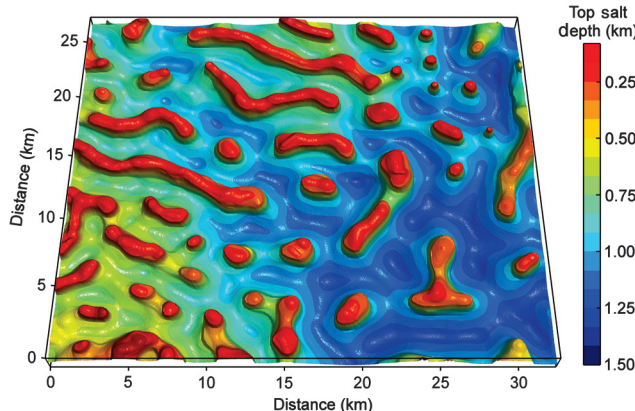


Figure 12. Top-salt surface deduced from combined focused inversion of  $G_{zz}$  and 2D seismic interpreted top-salt horizons.

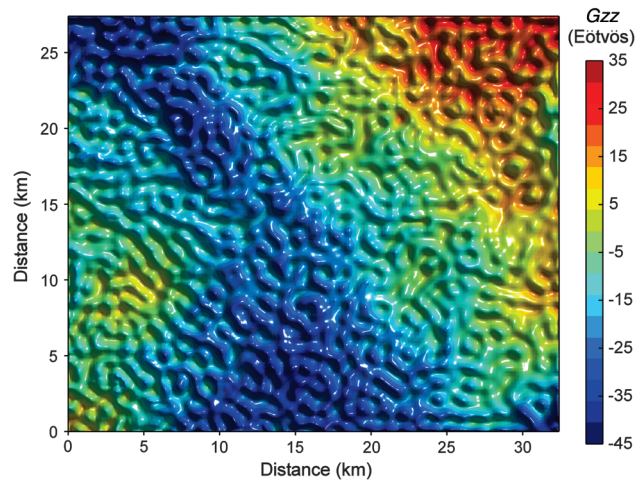


Figure 13. Near-surface corrected  $G_{zz}$ .

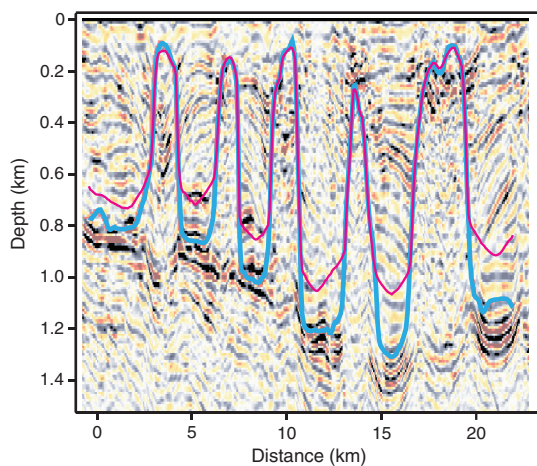


Figure 14. Comparison of inverted surface with depth-migrated seismic data along profile B–B'. Thick blue line: original top-salt pick used in the inversion, red line: result of inversion, background image shows 2D seismic.

is difficult to identify and subject to human error in these regions. To express this a priori uncertainty, the depth horizons were weighted with a depth-dependent function having a maximum of 1.0 for the shallowest and a minimum of 0.2 for the deepest depth estimate. These weights entered the optimization via the  $\mathbf{W}$  matrix in equation 17.

The focused and TV regularized inversion is shown in Figure 12 and represents our best estimate of the top-salt surface. The subsequent near-surface corrected  $G_{zz}$  (the unfiltered residual), shown in Figure 13, has removed both the high-frequency and long-wavelength signals from the salt-limestone interface and leaves high-frequency noise variation together with long-wavelength signal. The high-frequency component is made up from near-surface geological noise together with measurement noise, and the long-wavelength components represent the unmodeled deeper geology. Importantly, there are few traces of the salt bodies in this residual showing that the inverted surface is compatible with the measured data. In the right-hand side region away from the seismic profiles, there is a lack of control on the low-order surface trends, and consequently, it is not treated with as much confidence as the region where both data sets were contributing to the inverted surface.

The fit to the seismic derived depth data, Figure 14, shows that the inversion followed these data closely along the shallow tops of the salt bodies, but has larger departures in between. The depth-migrated and interpreted seismic data were deemed to be less reliable in these deeper regions and therefore weighted less by the depth-dependent weighting function in favor of fitting to the gravity gradient data. At the locations of some of the seismic data, the surface shows a scar where the depth data are wanting to pull up the surface from a slightly deeper level desired by the gravity gradient data. Inaccuracies in the inversion are most likely the result of an oversimplified model; the measured gravity gradient signal is made up from several contributing layers rather than just the modeled limestone-salt interface. The focused inversion mitigates the effect of the deeper layers, but unmodeled signal from shallow features in the weathering layer that are coincident with the salt bodies will cause errors in the inversion. In reality, the density-contrast does not follow a simple exponential law, especially above the salt bodies where cuvettes have formed. A more comprehensive approach is to model more layers or have a more sophisticated density versus depth variation.

## CONCLUSIONS

The nonlinear inversion of potential field data into surfaces that separate regions of prescribed rock type has been described. The implementation, being spatially based, allows depth information and regularization to be incorporated in a relatively straightforward manner. Such features are essential to mitigate the nonuniqueness problem when inverting potential field data alone. In the synthetic test and the field example, we showed how gravity gradient data can be inverted with interpreted horizons from depth-migrated 2D seismic to form a fully 3D geologic surface. The depth information was incorporated by employing a gridding style inverse interpolation method, which allowed the surface to be fitted to these data rather than being constrained by them. This provided the flexibility for the inversion to accommodate uncertainties in the depth estimates when simultaneously fitting a surface to be compatible with the field data. By choosing the appropriate form of regularization,

the inverted surface can be made to be geologically realistic. In the case of inverting for salt bodies, we found that total variation regularization was appropriate. By incorporating a high-pass filter into the inversion algorithm, the long-wavelength interference in the gravity gradient data originating from deeper geology was suppressed, forcing the low-order trends in the top-salt surface to be controlled by the depth horizons. The inversion therefore focused its fit to the high-frequency content of the gravity gradient data which is unique to the near-surface targets and ignored the ambiguous long-wavelength signal.

Not benefiting from the computational efficiency found in Fourier implementations of surface inversion, our spatially based method required approximations to make the problem solvable on standard desktop computers. Such approximations allowed a sparse representation for the internal matrices and, coupled with optimized multithreaded matrix operations, resulted in an efficient inversion engine based around the conjugate gradient algorithm. The time required to solve the field example, which had  $1.6 \times 10^5$  variables and  $2.5 \times 10^4$  input data points, was less than 10 minutes on an Intel 3.33 GHz i7 processor based desktop PC.

## ACKNOWLEDGMENTS

We thank Maurel & Prom for permission to show parts of the Gabon data and interpretation. Thanks are also due to J. Bain, V. Barbosa, D. FitzGerald, S. Goussev, B. Lahmeyer, X. Li, and other anonymous reviewers for their comments and suggestions on earlier versions of this article.

## APPENDIX

### EQUATIONS FOR $g_z$ AND $G_{zz}$ FROM A RECTANGULAR PRISM AND THEIR DERIVATIVES WITH RESPECT TO THE BOTTOM DEPTH

The rectangular prism is aligned along the  $x$ -,  $y$ -,  $z$ -axes and bounded by limits  $x_1, x_2, y_1, y_2, z_1, z_2$ . The origin of the coordinate system is placed at the field point. The density of the block is  $\rho$  and the gravitational constant is represented by  $G$ . The units for  $g_z$  and  $G_{zz}$  are mGal and Eötvös (E), respectively.

$$\begin{aligned} \text{Field} = & K(x_1, y_1, z_1) - K(x_2, y_1, z_1) - K(x_1, y_2, z_1) \\ & + K(x_2, y_2, z_1) - K(x_1, y_1, z_2) + K(x_2, y_1, z_2), \\ & + K(x_1, y_2, z_2) - K(x_2, y_2, z_2) \\ \frac{\partial \text{Field}}{\partial z_1} = & -dK(x_1, y_1, z_1) + dK(x_2, y_1, z_1) \\ & + dK(x_1, y_2, z_1) - dK(x_2, y_2, z_1), \end{aligned} \quad (\text{A-1})$$

where, for  $g_z$  field,

$$\begin{aligned} K(x, y, z) = & 10^5 G \rho \left( z \tan^{-1} \left( \frac{xy}{zR} \right) - x \log(R + y) - y \log(R + x) \right), \\ dK(x, y, z) = & 10^5 G \rho \tan^{-1} \left( \frac{xy}{zR} \right), \\ R = & \sqrt{x^2 + y^2 + z^2}, \end{aligned} \quad (\text{A-2})$$

and for  $G_{zz}$  field,

$$\begin{aligned} K(x, y, z) = & 10^9 G \rho \tan^{-1} \left( \frac{xy}{zR} \right), \\ dK(x, y, z) = & \frac{10^9 G \rho xy (x^2 + y^2 + 2z^2)}{(x^2 + z^2)(y^2 + z^2)R}, \\ R = & \sqrt{x^2 + y^2 + z^2}. \end{aligned} \quad (\text{A-3})$$

## REFERENCES

- Acar, A., and C. R. Vogel, 1994, Analysis of bounded variation penalty methods for ill-posed problems: *Inverse Problems*, **10**, 1217–1229, doi: [10.1088/0266-5611/10/6/003](https://doi.org/10.1088/0266-5611/10/6/003).
- Barbosa, V. C. F., and J. B. C. Silva, 2010, Reconstruction of geologic bodies in depth associated with a sedimentary basin using gravity and magnetic data: *EGM International Workshop*.
- Barbosa, V. C. F., J. B. C. Silva, and W. E. Medeiros, 1997, Gravity inversion of basement relief using approximate equality constraints on depths: *Geophysics*, **62**, 1745–1757, doi: [10.1190/1.1444275](https://doi.org/10.1190/1.1444275).
- Barnes, G. J., J. Barraud, J. Lumley, and M. Davies, 2008, Advantages of multi-tensor high resolution gravity gradient data: 78th Annual International Meeting, SEG, Expanded Abstracts, 3587–3590.
- Barnes, G. J., and J. M. Lumley, 2011, Processing gravity gradient data: *Geophysics*, **76**, no. 2, I33–I47, doi: [10.1190/1.3548548](https://doi.org/10.1190/1.3548548).
- Barnes, G. J., J. M. Lumley, P. Houghton, and R. Gleave, 2011, Comparing gravity and gravity gradient surveys: *Geophysical Prospecting*, **59**, 176–187, doi: [10.1111/gpr.2010.59.issue-1](https://doi.org/10.1111/gpr.2010.59.issue-1).
- Barraud, J., F. Assouline, N. Dyer, and J. Watson, 2010, Interpretation of gravity gradiometry and integration with PSDM workflow — Imaging sub-salt structures in Gabon: 72nd Conference & Exhibition, EAGE, Extended Abstracts.
- Chakravarthi, V., and N. Sundararajan, 2007, 3D gravity inversion of basement relief — A depth dependent density approach: *Geophysics*, **72**, no. 2, 123–132, doi: [10.1190/1.2434780](https://doi.org/10.1190/1.2434780).
- Dransfield, M., 2010, Conforming Falcon gravity and the global gravity anomaly: *Geophysical Prospecting*, **58**, 469–483, doi: [10.1111/j.1365-2478](https://doi.org/10.1111/j.1365-2478).
- Fedi, M., and A. Rapolla, 1999, 3-D inversion of gravity and magnetic data with depth resolution: *Geophysics*, **64**, 452–460, doi: [10.1190/1.1444550](https://doi.org/10.1190/1.1444550).
- Fullagar, P. K., G. A. Pears, and B. McMonnies, 2008, Constrained inversion of geologic surfaces — Pushing the boundaries: *The Leading Edge*, **27**, 98–105, doi: [10.1190/1.2831686](https://doi.org/10.1190/1.2831686).
- Guo, L., X. Meng, and L. Shi, 2011, Gridding aeromagnetic data using inverse interpolation: International workshop on gravity, electrical & magnetic methods and their applications, GEM 2011, Expanded abstracts.
- Jacobsen, B. H., 1988, Reply to discussion on: “A case for upward continuation as a standard separation filter for potential field maps”: *Geophysics*, **53**, 723–724.
- Lane, R., 2011, Building on 3D geological knowledge through gravity and magnetic modelling workflows at regional to local scales: 2011 SEG honorary lecture series.
- Li, X., 2010, Efficient 3D gravity and magnetic modelling: *EGM International Workshop*.
- Li, Y., and D. W. Oldenburg, 2003, Fast inversion of large-scale magnetic data using wavelet transforms and a logarithmic barrier method: *Geophysical Journal International*, **152**, 251–265, doi: [10.1046/j.1365-246X.2003.01766.x](https://doi.org/10.1046/j.1365-246X.2003.01766.x).
- Lima, W. A., C. M. Martins, J. B. C. Silva, and V. C. F. Barbosa, 2011, Total variation regularization for depth-to-basement estimate: Part 2 — Physiogeologic meaning and comparisons with previous inversion methods: *Geophysics*, **76**, no. 14, I13–I20, doi: [10.1190/1.3524547](https://doi.org/10.1190/1.3524547).
- Martins, C. M., W. A. Lima, V. C. F. Barbosa, and J. B. C. Silva, 2011, Total variation regularization for depth-to-basement estimate: Part 1 — Mathematical details and applications: *Geophysics*, **76**, I1–I12, doi: [10.1190/1.3524286](https://doi.org/10.1190/1.3524286).
- Medeiros, W. E., and J. B. C. Silva, 1996, Geophysical inversion using approximate equality constraints: *Geophysics*, **61**, 1678–1688, doi: [10.1190/1.1444086](https://doi.org/10.1190/1.1444086).
- Oldenburg, D. W., and D. A. Pratt, 2007, Geophysical inversion for mineral exploration: A decade of progress in theory and practice, in B. Milkereit, ed., *Proceedings of Exploration 07: Fifth decennial international conference on mineral exploration*, 61–95.
- Parker, R. L., 1973, The rapid calculation of potential anomalies: *Geophysical Journal of the Royal Astronomical Society*, **31**, 447–455.
- Pilkington, M., 2006, Joint inversion of gravity and magnetic data for two-layer models: *Geophysics*, **71**, no. 3, L35–L42.

- Portniaguine, O., and M. S. Zhdanov, 1999, Focusing geophysical inversion images: *Geophysics*, **64**, 874–887, doi: [10.1190/1.1444596](https://doi.org/10.1190/1.1444596).
- Portniaguine, O., and M. S. Zhdanov, 2002, 3-D magnetic inversion with data compression and image focusing: *Geophysics*, **67**, 1532–1541, doi: [10.1190/1.1512749](https://doi.org/10.1190/1.1512749).
- Press, W. H., S. A. Teukolsky, W. T. Vetterling, and B. P. Flannery, 1997, *Numerical recipes in C*, 2nd ed.: Cambridge University Press.
- Silva Dias, F. J. S., V. C. F. Barbosa, and J. B. C. Silva, 2011, Adaptive learning 3D gravity inversion for salt-body imaging: *Geophysics*, **76**, no. 3, I49–I57, doi: [10.1190/1.3555078](https://doi.org/10.1190/1.3555078).
- Wan, L., and M. S. Zhdanov, 2008, Focusing inversion of marine full-tensor gradiometry data in offshore geophysical exploration: 78th Annual International Meeting, SEG, Expanded Abstracts, 751–755.
- Zhdanov, M. S., 2002, *Geophysical inverse theory and regularization problems*: Elsevier.
- Zhdanov, M. S., R. G. Ellis, and S. Mukherjee, 2004, Regularized focusing inversion of 3D gravity tensor data: *Geophysics*, **69**, 925–937, doi: [10.1190/1.1778236](https://doi.org/10.1190/1.1778236).